

# Dynamical Spreading Under Power Law Potential

Ido Fanto,<sup>1</sup> Yuval Rosenblum,<sup>1</sup> Ori Harel,<sup>1</sup> and Naomi Oppenheimer<sup>1</sup>

<sup>1</sup>*School of Physics and Astronomy and the Center for Physics and Chemistry of Living Systems, Tel Aviv University, Tel Aviv 6997801.\**

(Dated: February 11, 2025)

We investigate the dynamic spreading of a dense suspension of particles under power law repulsive potentials decaying as  $1/r^k$ . We find analytically that the particles spread in a self-similar form, where the radius grows with time as  $t^{1/(k+2)}$ . Our results closely align with experiments of paramagnetic colloidal particles under an external magnetic field interacting via a  $1/r^3$  potential. We further substantiate the theory by molecular dynamic simulations of thousands of particles in one and two dimensions. The simulations reveal a rich diversity of behaviors contingent on the value of  $k$ . Specifically, for  $k > D - 2$  (where  $D$  is the dimension), the density is centered in the middle, for  $k = D - 2$ , density is uniform, and for  $k < D - 2$ , there is an aggregation of particles at the edge of the suspension. When two or more such suspensions are placed near each other, the system retains a power-law memory of its initial state, resulting in a particle-free zone at the interface of the merging populations.

Power-law potentials influence many phenomena governing our lives. They are the reason the Earth orbits the sun and the cause our hair stands on end on a dry winter day; it is how charged particles interact with each other and why a compass points to the north [1]. As such, it is no wonder that power-law potentials have been the subject of numerous studies. Usually, the focus is on equilibrium configurations, where the density of the particles is static and thermal fluctuations are present ([2–4]). In this paper, we analyze the deterministic dynamics of an initially concentrated suspension of particles as they spread in free space. We assume that the system is overdamped and that particles interact with each other by a power-law potential  $U \propto 1/r^k$ . Such systems are called Riesz gases [5, 6]. The exponent,  $k$ , determines the nature of the interaction and can take values between  $(-2, \infty]$ . It is possible to classify the interaction by the range of the potential — for  $k > D$  the interaction is short-ranged, integration of the potential across space converges, and particles interact with their nearest neighbors; for  $k \leq D$  the interaction is long-ranged, and spans the system [7, 8]. As we will show, the density profile, in fact, depends on a different characterization and is origin-centered for  $k > D - 2$ , constant for  $k = D - 2$ , and boundary-centered, resembling the coffee-ring effect [9], for  $k < D - 2$ . In what follows, we will derive the scaling dynamics of the suspension and show that the density has a self-similar solution of the form

$$\rho(r, t) = At^\gamma f\left(\frac{Br}{t^\beta}\right) \quad (1)$$

$$\text{with } \gamma = -\beta D \text{ and } \beta = \frac{1}{k+2},$$

where  $\beta = 1/(k+2)$  irrespective of dimension. We

will verify this result by observing experimentally the two-dimensional (2D) spreading of paramagnetic colloids under an external, perpendicular, magnetic field that creates a dipole-dipole repulsion that scales as  $1/r^3$  [10, 11]. We observe that the radius grows as  $t^{1/5}$ , as predicted by the scaling in Eq. 1. The density profiles at different times collapse to a single curve given by Eq. 1. We further verify our results using Molecular Dynamics (MD) simulations of thousands of particles. We go on to study the density profiles for different power-laws in 2D (and 1D in the Supplementary Information).

We study systems in the overdamped regime, such that the velocity is directly proportional to the force through the mobility  $\mu$ ,  $\mathbf{v} = \mu\mathbf{F} \sim 1/r^{k+1}$ . The velocity of each particle is determined by the contribution to the force acting on it from all other particles. For a system of  $N$  particles, the velocity of the  $i^{\text{th}}$  particle can be written in the following discrete form

$$\mathbf{v}_i(\mathbf{r}_i) = v_0 \sum_{j \neq i}^N \frac{l^{k+1}}{|\mathbf{r}_i - \mathbf{r}_j|^{k+1}} \hat{\mathbf{r}}_{ij}, \quad (2)$$

with  $v_0 = \mu F_0$  being the typical magnitude of the velocity, and  $l$  is a length simply used to make the force dimensionless. To test the collective dynamics experimentally, we used super-paramagnetic particles made of polystyrene (PS) or Silicon dioxide ( $\text{SiO}_2$ ) with diameters between 5-12  $\mu\text{m}$ . Both types of particles have nanoparticles of iron oxide embedded in them. The particles are electrostatically stabilized to avoid short-range attraction and aggregation. Costume-built Helmholtz coils are placed such that they generate a uniform magnetic field perpendicular to the plane of the sample. An illustration of the setup can be seen in the SI. The field magne-

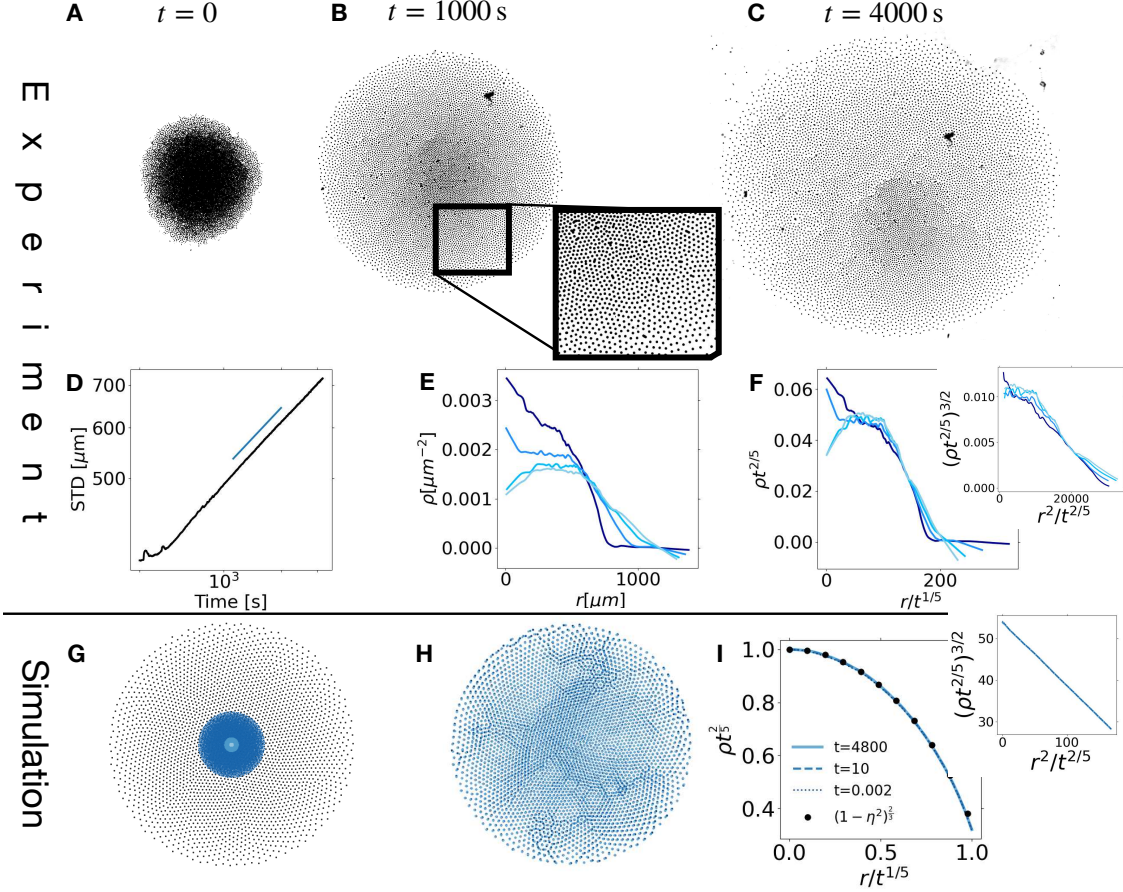


FIG. 1. Experiments and simulations of particles spreading under a  $1/r^3$  potential. (a-c) snapshots at three different times. (a) initially, (b) after 16 minutes, inset shows a zoom-in showing the triangular organization of the particles, and (c) after about one hour. (d) the standard deviation as a function of time showing  $R \sim t^{1/5}$  in line with the theoretical prediction, (e) density as a function of distance at four different times ( $t = 1500, 3000, 4500, 5500$ s) (f) rescaled-density with respect to  $t^{2/5}$  as a function of the self-similarity parameter  $r/t^{1/5}$  showing the four curves collapse to a single one. The inset plots  $(\rho t^{2/5})^{3/2}$  versus  $\eta^2$ , which, according to the theory, should be linearly decreasing. (g-i) results from molecular dynamics simulations of 3000 particles with a  $1/r^3$  potential showing the same spreading as in the experiment. (g) Snapshots of the simulation at three different times ( $t = 0.002, 10, 4800$ ). (h) The same snapshots from (g) but rescaled according to Eq. 1. (i) rescaled average density showing a collapse to a single curve and a fit to the theoretical prediction given by Eq. 13. The inset plots  $(\rho t^{2/5})^{3/2}$  versus  $\eta^2$  showing the linear predicted trend.

tizes the particles, creating dipole-dipole magnetic repulsion of the form  $U(r) \propto 1/r^3$ . More precisely

$$U = \frac{\mu_0}{4\pi|\mathbf{r}|^3} [\mathbf{m}_1 \cdot \mathbf{m}_2 - 3(\mathbf{m}_1 \cdot \hat{\mathbf{r}})(\mathbf{m}_2 \cdot \hat{\mathbf{r}})], \quad (3)$$

where  $\mathbf{m}_1$  ( $\mathbf{m}_2$ ) are the magnetic moments of the first (second) particle, and  $\mu_0$  is the magnetic constant.

The experiment is conducted as follows: we start by creating a sample in a capillary tube (0.2mm x 6mm x 50mm) with a ratio of between (1:300) to (1:2000) microliters of particles to deionized water. To concentrate the particles, we use a bar magnet,

congregating particles where the magnetic field is strongest. We view the sample using a microscope (Nikon Eclipse Ti2) with  $\times 4$  magnification lens and 0.2 NA. A uniform magnetic field of around 4-5 mT was generated using a pair of Helmholtz coils connected to a power supply. We record the spreading of the particles at one frame per second, using a camera (Nikon-kinetix-m-c). In Fig. 1A-C the time evolution of the suspension is shown. We can indeed observe that the colloids repel each other, and the suspension spreads. The resulting expanding drop is very different from a drop of passive thermal particles — for thermal particles, the boundary of a

drop becomes diffused over time; here, the boundary is sharp, and the concentration is zero beyond a certain point (see Fig. 1B and C) [12–14]. Furthermore, the diffusion coefficient for the PS particles was found to be  $\mathcal{D} = 0.022 \left[ \frac{\mu\text{m}^2}{\text{sec}} \right]$  (see SI) and the Péclet number  $Pe \sim 260 \gg 1$ , indicating that diffusion is negligible in regard to the dipole-dipole interaction. We analyzed the experiment in Python using Trackpy [15] to locate the positions of the particles. Fig 1D is the standard deviation as a function of time, showing that  $\text{STD}(t) \propto R(t) \propto t^{\frac{1}{5}}$ , where  $R$  is the radius of the drop. The density of the suspension was calculated using Voronoi tessellation, taking the density of particle  $i$  positioned at  $\mathbf{r}$  to be the inverse of its Voronoi area,  $\rho(\mathbf{r}) = 1/A_{\text{cell}}^i$ . Fig. 1E shows a radial average of the distribution as a function of distance from the center at four different frames ( $t = 1500, 3000, 4500, 5500$  s). The distribution is isotropic, and, upon rescaling the data according to Eq. 1, plots at different times collapse to a single universal curve, see Fig. 1F.

To further validate the results, we numerically propagate Eq. 2 using MD simulations. We used an 8th-order Runge-Kutta scheme with an adaptive timestep. We place thousands of point-like particles randomly in an initial disk of radius  $R_0 = 1$  and let them evolve. Fig 1G is an overlay of four snapshots from a simulation of a power law potential with  $k = 3$ , similar to the experiment. By re-plotting the snapshots while rescaling the radius according to Eq. 1, we see that they completely overlap, as seen in Fig. 1H. The shape of the density profile thus remains the same, and the system is indeed self-similar. This is further evident in Fig. 1I, where the radially averaged densities are presented, and all, when rescaled, fall on the same curve. The particles in both experiment and simulation show the formation of a triangular Wigner lattice[16], see, for example, the inset in Fig. 1B, and the SI. Since our system is unbounded, unlike a regular Wigner lattice, the distance between lattice sites varies, and defects emerge (perhaps resembling defects on curved surfaces [17, 18]).

Let us describe the dynamics of two particles before outlining the dynamics of a large number of particles,  $N$ . Consider two particles that are repelled by the potential  $U = U_0 t^k / r^k$ . In the overdamped case, the particles move apart at a distance that grows as  $r \propto t^{\frac{1}{k+2}}$ . As we will show, the same scaling also appears in the ensemble limit. This is reminiscent of thermal diffusion in which a single Brownian particle has a standard deviation of  $\sqrt{t}$ , similar to an ensemble of particles. But, it is surprising since Brown-

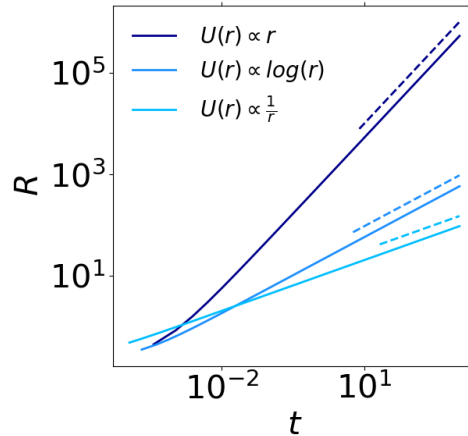


FIG. 2. Radius versus time for  $k = (-1, 0, 1)$  in a simulation of 10000 particles, along with the theoretical scaling,  $R(t) \propto t^{\frac{1}{k+2}}$ , shown as a dashed line.

ian particles are non-interacting, whereas power-law repulsion involves many-body interactions, which could have been expected to change the scaling (as indeed, sometimes they can [14]).

To derive the self-similarity scaling, we will coarse-grain the dynamical equations. Considering  $N$  particles that adhere to a power law potential, the continuity equation reads

$$\frac{\partial \rho}{\partial t} + \nabla \cdot (\rho \mathbf{v}) = 0, \quad (4)$$

where  $\mathbf{v}$  is the velocity, and  $\rho$ , the density, defined by  $\rho(\mathbf{r}) = \sum_j^N \delta(\mathbf{r}_j - \mathbf{r})$ . Let us work with dimensionless variables such that  $v \rightarrow v/v_0$ ,  $\mathbf{r} \rightarrow \mathbf{r}/R_0$ ,  $R(t) \rightarrow R/R_0$ , and  $\rho \rightarrow \rho/\rho_0$ , with  $R_0$  being the initial radius of the suspension, and  $\rho_0 = N/R_0^D$  is the initial density. For the isotropic initial conditions that we consider, the equation becomes,

$$\frac{\partial \rho}{\partial t} + \frac{1}{r^{D-1}} \frac{\partial(\rho r^{D-1} v)}{\partial r} = 0. \quad (5)$$

where  $v$  is the radial velocity. The number of particles is constant, giving a constraint

$$\text{const} = \Omega_D \int_0^\infty \rho(r, t) r^{D-1} dr, \quad (6)$$

where  $\Omega_D$  is the volume of a  $D - 1$  dimensional unit sphere. Plugging the self-similar ansatz,  $\rho(r, t) = At^\gamma f\left(\frac{Br}{t^\beta}\right)$ , and requiring that the solution must not depend explicitly on time, gives

$$\gamma = -\beta D. \quad (7)$$

The value of  $\beta$  will be derived from the potential  $U(r) \propto 1/r^k$ . We will begin by taking Eq. 2 to the continuum limit,

$$\mathbf{v}(\mathbf{r}) = \int_0^R \frac{\mathbf{r} - \mathbf{r}'}{|\mathbf{r} - \mathbf{r}'|^{k+2}} \rho(\mathbf{r}') d^D r'. \quad (8)$$

Using a non-dimensional variable  $\eta$ , where  $\eta = \frac{Br}{t^\beta}$ , we get that Eq. 8 together with Eq. 5 turn into an integral equation for  $f$ , the rescaled density, which depends only on the self-similar variable  $\eta$ . This happens if the exponent,  $\beta$ , is given by

$$\beta = \frac{1}{k+2}, \quad (9)$$

irrespective of dimension. The integral equation for the rescaled self-similar density,  $f$  is ,

$$\eta = \Gamma \int_0^{\eta_B} \frac{\eta - \eta'}{|\eta - \eta'|^{k+2}} f(\eta') d^D \eta' \cdot \hat{r}, \quad (10)$$

where the upper boundary of integration is now  $\eta_B = \frac{BR}{t^\beta}$ , and we defined  $\Gamma = B^{k+2-D} A(k+2)$ . Note that  $k$  can take values from  $(-2, \infty]$  since a negative  $\beta$  is not physical as it implies that  $r \rightarrow \infty$  is equivalent to  $t \rightarrow \infty$  and not  $t \rightarrow 0$ . Now that we have found that  $\beta = 1/(k+2)$  and  $\gamma = -\beta D$ , as written in Eq. 1, the density of the suspension can be renormalized according to the self-similar ansatz, i.e.  $\rho(r, t) = At^{-D/(k+2)} f\left(\frac{Br}{t^{1/(k+2)}}\right)$ . To put things more explicitly, even without solving Eq. 10 and finding the steady-state distribution,  $f$ , we can say two things exactly — in a suspension of repulsive particles with a power-law potential  $U \sim 1/r^k$ : (a) The radius of the suspension,  $R$ , grows with time as  $t^{1/(k+2)}$ , independent of the dimension. (b) The density profile is self-similar with  $\eta \propto r/t^{1/(k+2)}$  and its amplitude decreases with time as  $t^{-D/(k+2)}$ . We have shown this to be true in Fig. 1, for both experiments and simulations with  $k = 3$ . To further support the first claim, Fig. 2 shows the radius as a function of time taken from simulations of thousands of particles for  $k = (-1, 0, 1)$  along the theoretical predictions  $t^{1/(k+2)}$ .

We now turn to describing the steady-state density profiles. We have already seen an example of the density profile for a short-range power law,  $k = 3$ , in 2D, in Fig. 1. We now show simulation results for the density profiles in the case of a long-range power law ( $k \leq D$ ). Fig 3 plots the steady-state density profiles for three different values of the potential,  $k = (-1, 0, 1)$ , as well as their angular average at different times, and the rescaled density according to the self-similar variables given by Eq. 1. The re-

sults presented in Fig. 3 show vastly different density profiles depending on the values of  $k$ . These values of  $k$  are different from those that characterize short-ranged ( $k > D$ ) and long-ranged ( $k \leq D$ ) behaviors. The short versus long-ranged nature is related to the behavior of the potential energy and whether it is finite or diverges at infinity, whereas the density profile has a stricter condition. A long-ranged potential with  $k = 1$  in 2D is centered at the origin (as we have shown in Fig. 3A), the same goes for the short-ranged potential with  $k = 3$  as is shown in Fig. 1. Whereas the long-ranged pears  $k = 0$  and  $k = -1$  behave differently, see Fig. 3B and C. This means that both a long-ranged potential (e.g.  $k = 1$ ), and a short-ranged potential ( $k = 3$ ), result in an origin-centered density, but not all long-ranged potentials are origin centred.

We have tested simulations in 1D and 2D and can divide the profiles into three categories: (i) origin-centered for  $k > D - 2$ , (ii) constant profile at  $k = D - 2$ , and (iii) boundary-centered for  $k < D - 2$ . Systems that interact via  $k = D - 2$  are termed a ‘‘Coulomb gas’’, or a log-gas in 2D [2, 19]. The boundary-centered density profile is referred to in the literature as the ‘‘Evaporation Catastrophe’’ [20] and is attributed to the potential being too repulsive at infinity. As a side note, we can also notice in Fig. 2 that for  $k = 0$  i.e.  $U(r) \propto \log(r)$ , the suspension grows with the square root of time, similar to thermal diffusion, even though for diffusion, there are no interactions between particles, and here the particles are purely repulsive. We can extend this analogy to more values of  $k$ , some of which can be seen in Fig. 2. The dynamics, regardless of the dimension, is: (a) subdiffusive for  $k > 0$ , (b) diffusive for  $k = 0$ , (c) superdiffusive for  $-1 < k < 0$ , and (d) ballistic for  $k = -1$ .

**Density for short-ranged interactions.** For short-range interactions, i.e., in the limit  $k > D$ , we follow Ref. [13] but take a slightly different route. The velocity at position  $\boldsymbol{\eta}$  depends on integration over all of space, but in the short-ranged limit, faraway particles will have negligible contributions. Thus, we perform a Taylor expansion of the rescaled density  $f(\boldsymbol{\eta}')$  around  $\boldsymbol{\eta}$ ,

$$f(\boldsymbol{\eta}') = f(\boldsymbol{\eta} + \mathbf{s}) \approx f(\boldsymbol{\eta}) + \mathbf{s} \cdot \vec{\nabla} f(\boldsymbol{\eta}) + \dots, \quad (11)$$

where  $\mathbf{s} = \boldsymbol{\eta}' - \boldsymbol{\eta}$ . Since particle interactions decay quickly, we can extend the integration boundaries to the entire space for particles far enough from the boundary. This results in,

$$\eta \approx -\Gamma \int_0^\infty \frac{\mathbf{s}}{s^{k+2}} [f(\boldsymbol{\eta}) + \mathbf{s} \cdot \nabla f(\boldsymbol{\eta})] d^D s \cdot \hat{r}. \quad (12)$$

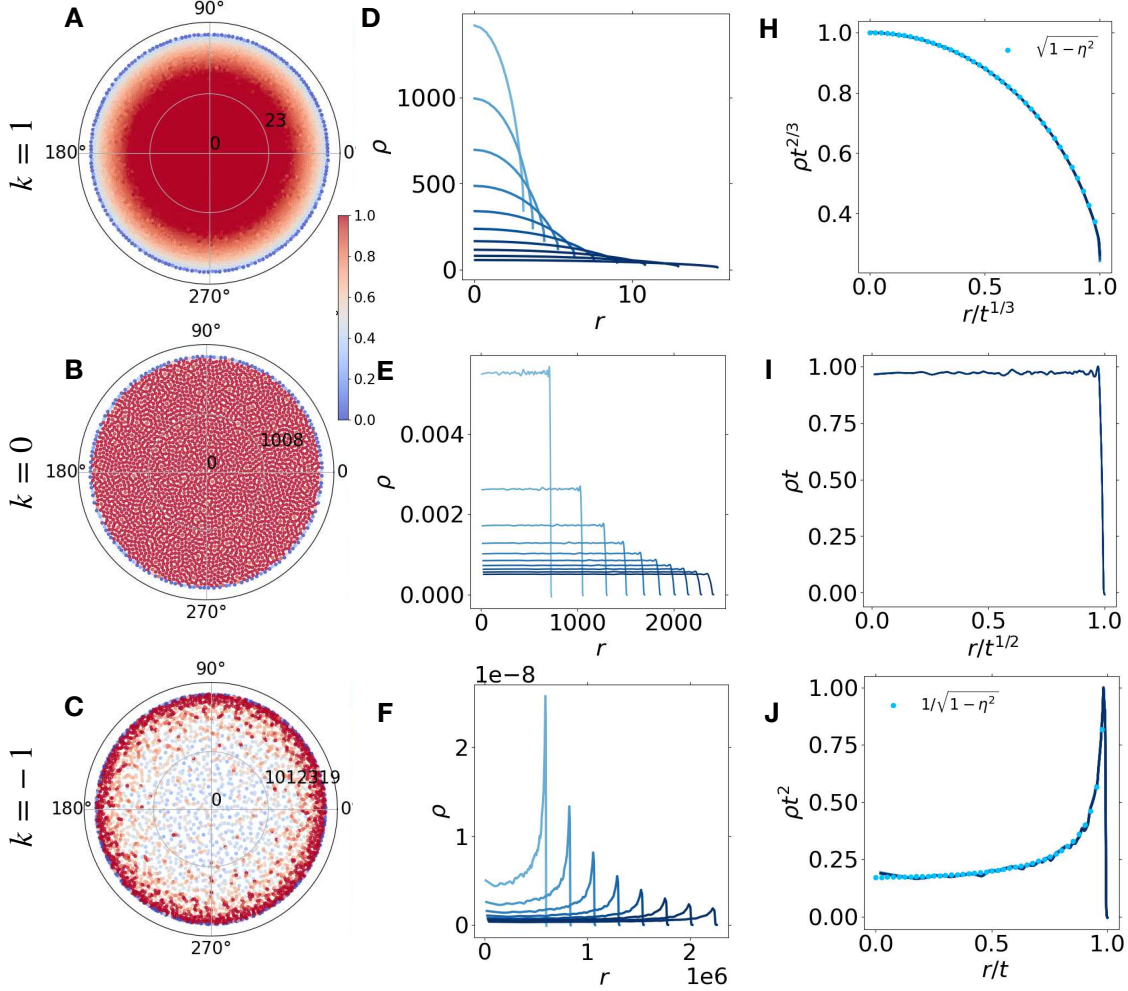


FIG. 3. Simulations in the long-range limit  $k < D$ . a–c snapshots of the distribution at steady-state, with color coding according to the density for (a)  $k = 1$ , (b)  $k = 0$ , and (c)  $k = -1$ . (d–f) Angular average of the density at 10 different times, with color going from light blue at early times to dark blue at later ones. (h–j) rescaled density according to  $\rho t^{2\beta}$  as a function of the self-similar variable  $\eta = r/t^\beta$ . Bright blue dots give the theoretical predictions given in Eq. 15

The first moment in Eq. 11 vanishes after integration from symmetry considerations. The angular integral in the resulting integral can be performed on a spherical surface using the identity  $\int \hat{s} \hat{s} d\Omega_D = \mathbf{I} S_D / D$ , where  $\hat{s} = \mathbf{s}/s$ , and  $\mathbf{I}$  is the identity tensor. The radial part of Eq. 12 is of the form  $\int_0^\infty s^{D-1-k} ds$ . It is crucial to resolve the divergence at the lower boundary. For that, we adopt the consideration in Refs. [21] [13] — it is highly unlikely for two repulsive particles in a dissipative medium to collide, so this divergence is not physical. An excluded area around each particle can be defined which is proportional to the mean distance between particles. In terms of the density, the lower boundary is  $r_{\text{exc}} = \alpha f^{-1/D}$ . By incorporating this excluded area, the integration in

Eq. 12 can be resolved, and we arrive at the first-order ODE,

$$\eta = -\frac{k}{2D} f^{k/D-1} \frac{df}{d\eta}, \quad (13)$$

where we defined  $B^{k-D+2} = \frac{k(k-D)}{2D(k+2)\Omega_D A \alpha^{D-k}}$ . This equation is, in fact, a result of nonlinear diffusion [14, 22–24]. The solution to Eq. 13 is

$$f(\eta) = (1 - \eta^2)^{\frac{D}{k}}. \quad (14)$$

The solution for the density given by Eq. 14 has what is known as compact support — the solution is strictly zero beyond some cutoff [12, 22, 24]. Figures 1F and 1I show an excellent agreement between

the experiment and the simulation and the analytic solution for  $k = 3$  in 2D. The inset shows a plot of  $(\rho t^{2/5})^{3/2}$  versus  $\eta^2 = r^2/t^{2/5}$ , which is linear as predicted by Eq. 14, combined with Eq. 1.

**Density for long-ranged interactions.** For long-ranged forces  $k < D$ , we will try to give some intuition to the unique profiles in Fig. 3A–C. As was already pointed out, the density profile in Fig. 3B and the supplementary information in 1D, indicate that for  $k = D - 2$ , the density is constant. A formal proof is given in Ref. [25]. Here, let us give some intuition. For any solution to be self-similar, the velocity must be proportional to the distance from the center,  $r$ . That is  $v \propto r$  (see SI for an example). Assuming a constant density in Eq. 8, the integral scales as  $r^{-k-1+D}$  equating it to  $r$ , gives  $k = D - 2$ . Thus, for a potential of  $U \sim 1/r^{D-2}$ , the density profile is spatially constant. We have yet to solve Eq. 10 for other values of  $k < D$ . A solution for 1D is given in [3, 25]. We hypothesize that a generalization to any dimension will have the following form

$$f(\eta) \propto (1 - \eta^2)^{\frac{k+2-D}{2}}. \quad (15)$$

This solution gives the correct result in 1D, as well as a constant profile when  $k = D - 2$  for any dimension. We also verified this result for  $k = -1, 0, 1$  in 2D, see Fig. 3G–I. Notice how Eq. 15 has the same form as Eq. 14 with a different power law.

**Colliding drops.** So far, we have only looked at the case of a single suspension expanding in free space. Let us examine qualitatively what happens when two or more populations collide. We simulate the collision by initiating the simulation with two or more suspensions separated by a certain distance so that they do not touch initially. We then let the system evolve. At some point, the suspensions meet. We ask, what is the density of the suspension as a function of time? All cases we examined appear to be absorbing; that is, the initial conditions do not matter, and the state is universal over time. However, we show that when  $k \geq D - 2$ , the system reaches the absorbing steady state exponentially, whereas for  $k < D - 2$ , the system remembers its initial state over long periods of time and reaches a steady state as a power law. Fig 4 presents results for the collision between two drops for the case of  $k = 3$ , which after a short period forms the expected isotropic steady-state, versus the case of  $k = -1$ , which has a particle-free zone that grows over time. On Fig. 4D and E we plot the particle-free zone as a function of time for both power-laws, showing how it grows for  $k = -1$  and shrinks for  $k = 3$ . Note that despite the growth of the particle-free zone for

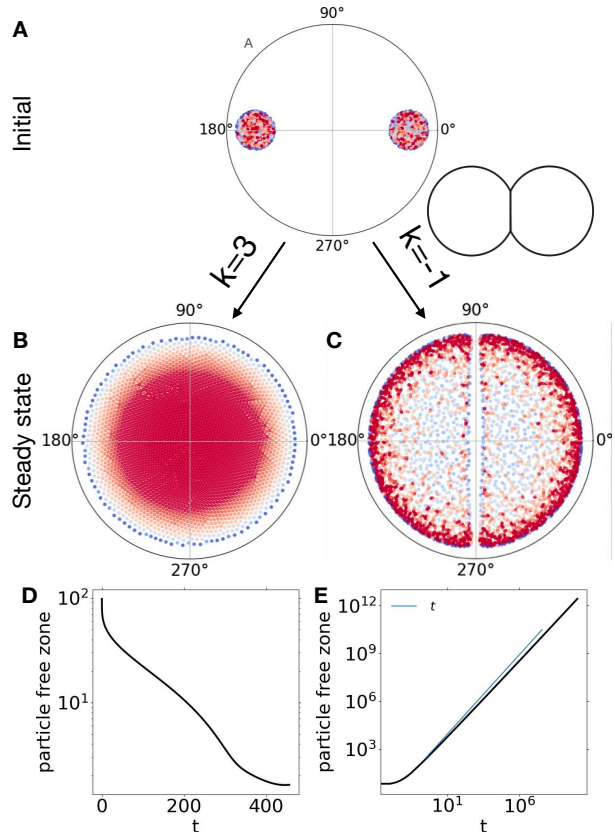


FIG. 4. Collision of two suspensions of  $N = 1500$  particles each, for  $k = 3$  (in b) and  $k = -1$  (in c). (a) the initial configuration (b) and (c) at  $(t = XXX)$ . (d) and (e) plots of the length of the corridor that does not contain particles between the two suspensions. Note how it shrinks almost exponentially for  $k = 3$ , and grows for  $k = -1$ .

$k = -1$ , it grows with a power-law that is slightly less than 1, i.e. less than the radius of a single suspension grows with time (see Fig. 2). Therefore, at very long times, the two suspensions will be indistinguishable from a single drop. Results for the collision between four populations are presented in the SI.

**Discussion.** We explored the self-similar dynamics of a dense ensemble of particles spreading in free space under a repulsive power-law potential. The density profile is given by  $At^{D/(k+2)}f(\eta)$ , with  $\eta = Br/t^{1/(k+2)}$  where  $f$  is always in the form of a semi-circle  $(1 - \eta^2)^\delta$ . This shape also appeared for short-ranged potentials with a cutoff [14]. The exponent changes according to the value of  $k$ : (i)  $\delta = D/k$  for short-ranged potentials ( $k > D$ ) and (ii)  $\delta = (k + 2 - D)/2$  for long-ranged potentials ( $k < D$ ). Dynamics in the short-ranged case can be approximated by a non-linear diffusion equation with a

diffusion coefficient that depends on the density to some power. Regular thermal diffusion is negligible since the Péclet number, which is a measure of advective motion relative to thermal diffusion, is very large  $Pe = va/D \sim 260$ , where  $a$  is the size of the particle, and  $D = 0.05\mu\text{m}^2/\text{s}$  is the measured thermal diffusivity of the particles (see SI). It is also interesting to note that the steady-state solution is always the same as the equilibrium distribution when a harmonic potential is confining the particles (see e.g. [3, 13]).

We observed that different density profiles arise depending on whether  $k$  is greater than, less than, or equal to  $D - 2$ . We also observed an interesting phenomenon for values of  $k < D - 2$  — when two or more suspensions collide, a particle-free zone is formed, and the system has a long-term memory of its initial state. The resulting shapes are reminiscent of soap bubbles, however, in soap bubbles [26], the interaction is attractive, leading to the aggregation of particles at the boundary. Whereas in Fig. 4C, the interaction is repulsive, and the boundary between the suspensions is particle-free.

While writing this manuscript, we became aware of a preprint [25], which gives the analytic result and scaling for long-ranged potentials. Our results are aligned with their predictions in that limit.

---

\* idofanto@mail.tau.ac.il

- [1] E. M. Purcell, *Electricity and magnetism* (Cambridge university press, 2013).
- [2] T. Leblé and S. Serfaty, *Inventiones mathematicae* **210**, 645 (2017).
- [3] S. Agarwal, A. Dhar, M. Kulkarni, A. Kundu, S. N. Majumdar, D. Mukamel, and G. Schehr, *Phys. Rev. Lett.* **123**, 100603 (2019).
- [4] R. Dandekar, P. Krapivsky, and K. Mallick, *Physical Review E* **107**, 044129 (2023).
- [5] M. Lewin, *Journal of Mathematical Physics* **63** (2022).
- [6] S. Serfaty, “Lectures on coulomb and riesz gases,” (2024), arXiv:2407.21194 [math-ph].
- [7] J. J. Binney, N. J. Dowrick, A. J. Fisher, and M. E. Newman, *The theory of critical phenomena: an introduction to the renormalization group* (Oxford University Press, 1992).
- [8] A. Campa, T. Dauxois, and S. Ruffo, *Physics Reports* **480**, 57 (2009).
- [9] R. D. Deegan, O. Bakajin, T. F. Dupont, G. Huber, S. R. Nagel, and T. A. Witten, *Nature* **389**, 827 (1997).
- [10] K. Zahn, R. Lenke, and G. Maret, *Physical review letters* **82**, 2721 (1999).
- [11] K. Zahn and G. Maret, *Physical Review Letters* **85**,

- 3656 (2000).
- [12] P. Rosenau and J. M. Hyman, *Physical Review Letters* **70**, 564 (1993).
- [13] A. A. Moreira, C. M. Vieira, H. A. Carmona, J. S. Andrade, and C. Tsallis, *Phys. Rev. E* **98**, 032138 (2018).
- [14] M. Y. Ben Zion and N. Oppenheimer, *Physical Review Letters* **132**, 238201 (2024).
- [15] D. B. Allan, T. Caswell, N. C. Keim, C. M. van der Wel, and R. W. Verweij, “soft-matter/trackpy: v0.6.4,” (2024).
- [16] E. Wigner, *Phys. Rev.* **46**, 1002 (1934).
- [17] W. T. Irvine, V. Vitelli, and P. M. Chaikin, *Nature* **468**, 947 (2010).
- [18] C. P. Kelleher, A. Wang, G. I. Guerrero-García, A. D. Hollingsworth, R. E. Guerra, B. J. Krishnatreya, D. G. Grier, V. N. Manoharan, and P. M. Chaikin, *Physical Review E - Statistical, Nonlinear, and Soft Matter Physics* **92**, 1 (2015), arXiv:1701.08801.
- [19] P. Minnhagen, *Reviews of Modern Physics* **59**, 1001 (1987).
- [20] G. Gallavotti, *Statistical mechanics: A short treatise* (Springer Science & Business Media, 1999).
- [21] C. M. Vieira, H. A. Carmona, J. S. Andrade, and A. A. Moreira, *Phys. Rev. E* **93**, 060103 (2016).
- [22] G. I. Barenblatt, *Prikl. Mat. Makh.* **16**, 67 (1952).
- [23] H. Stone, in *Nonlinear PDE's in Condensed Matter and Reactive Flows* (Springer, 2002) pp. 297–312.
- [24] L. G. Leal, *Advanced transport phenomena: fluid mechanics and convective transport processes*, Vol. 7 (Cambridge University Press, 2007).
- [25] P. Krapivsky and K. Mallick, arXiv preprint arXiv:2412.14875 (2024).
- [26] S.-P. Wang, A.-M. Zhang, Y.-L. Liu, S. Zhang, and P. Cui, *Journal of Hydrodynamics* **30**, 975 (2018).

## Supplementary

In this supplementary, we will show results from simulations in  $1D$ . The initial configuration in  $1D$  is that the particles are uniformly distributed on a line centered around the origin. We also provide additional experimental details and further results from colloids of different material and diameters.

### 1D simulation results

Fig. 5 shows that the size of the  $1D$  suspension of particles grows with time as  $t^{\frac{1}{4}}$  for  $k = 2$ , this is the same value that was achieved in  $2D$  further showing that the growth of the suspension is independent on the dimensionality of the system. The density in  $1D$  is calculated in the same manner as in  $2D$  with the exception of using the distance between particles instead of a Voronoi area. The density of each

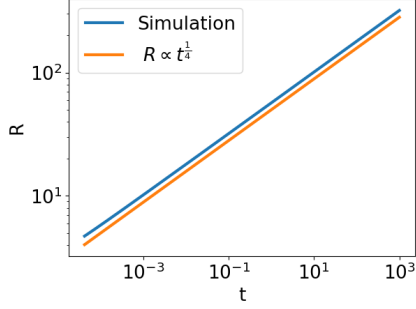


FIG. 5.  $R$  as a function of time in a  $1D$  suspension with  $k = 2$ :  $\beta = \frac{1}{4}$ .

particle is defined as half the distance from each of its neighbors.

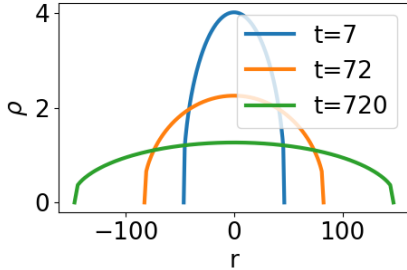


FIG. 6. Density profile at different times in a  $1D$  suspension with  $k=2$ .

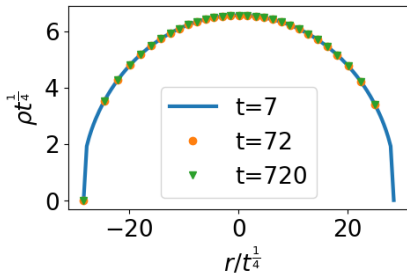


FIG. 7. Re-normalized Density profile at different times in a  $1D$  suspension with  $k=2$ .

Fig. 7 shows that using the self similar ansatz  $\rho(r, t) = At^\gamma f\left(\frac{Br}{t^\beta}\right)$ , all plots from Fig. 6 fall on the same curve. In Fig. 8 we can see that the solution derived for short ranged potentials ( $k > D$ ) is satisfied in  $1D$  as well.

In Fig. 9 and Fig. 11 we can see a constant density profile and a boundary-centered density profile in  $1D$ , respectively. Fig. 10 and Fig. 12 show the self-similar properties of these profiles.

We then tested collision between two ensembles in

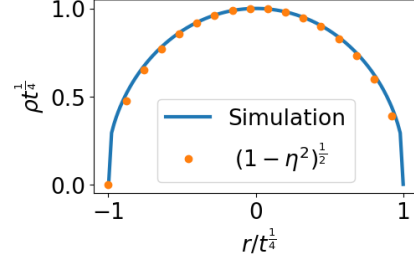


FIG. 8. Density profile from simulation of  $1D$  suspension, with  $k = 2 > D$  ( $\beta = 1/4$ ), alongside analytical solution. The data is normalized by the maximum value in each axis.

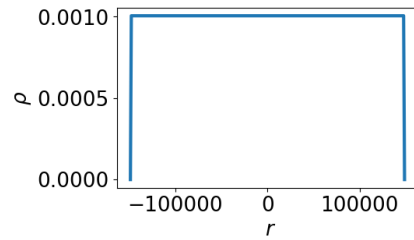


FIG. 9. Density profile from simulation of  $1D$  suspension, with  $k = -1 = D - 2$ . A constant density is observed.

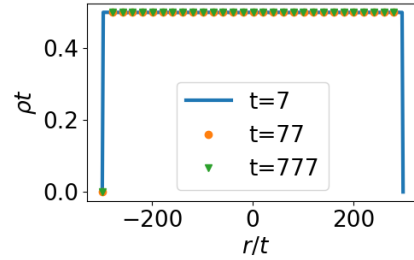


FIG. 10. Re-normalized density profile from simulation of  $1D$  suspension, with  $k = -1 = D - 2$  ( $\beta = 1$ ).

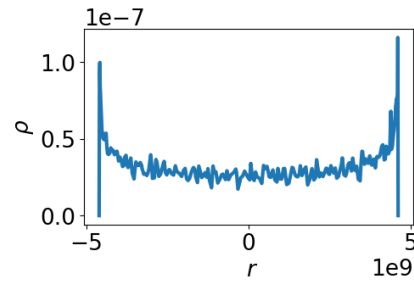


FIG. 11. Density profile from simulation of  $1D$  suspension, with  $k = -1.5 < D - 2$ . A boundary-centered density is observed.



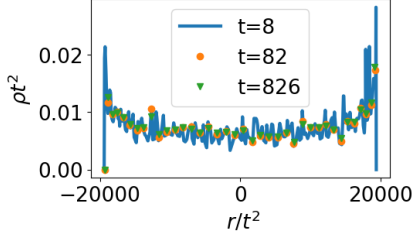


FIG. 12. Re-normalized density profile from simulation of 1D suspension, with  $k = -1.5 < D - 2(\beta = 2)$ .

1D. For the case of  $k < D - 2$  a particle-free zone is formed and maintained for a long duration as can be seen in Fig. 13. Note how the density falls to zero where the suspensions meet.

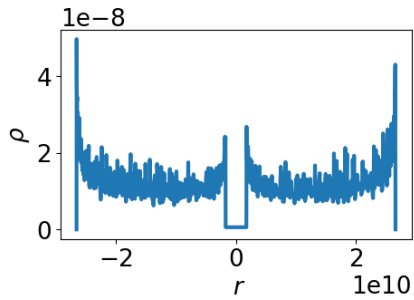


FIG. 13. Density profile from simulation of two 1D suspensions, with  $k = -1.5 < D - 2$ . A particle-free zone can be seen where the two suspensions meet.

Lastly, we tested collision between several ensembles in 2D. Results for the collision between 4 drops, where particles interact by  $U \sim r$  are presented in Fig. 14, and their resemblance to the boundary between four soap bubbles is shown.

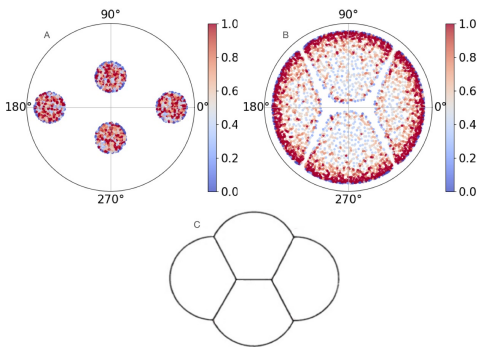


FIG. 14. Four drops, initially uniform and well distinct. Particles interact by a potential of the form  $U \sim r$ .

## Experimental setup and further experimental Results

**Preparing the Samples.** To begin the experiment, an overdamped suspension of paramagnetic particles was used (Polystyrene, or Silica with embedded iron oxide nanoparticles, 5% initial mass concentration). About one microliter of particles was removed from a concentrated, refrigerated suspension using a micropipette, and placed in a test tube. Distilled water was added (the ratio varied between 1 to a few hundred  $\mu L$  for PS 10 and a couple thousand for SiO 5, controlling the number of particles used). The sample was then placed in an ultrasonic cleaner to remove bubbles and separate aggregates. Throughout the preparation, the sample was mixed a few times.

The sample was then inserted into a capillary tube (primarily 6mm wide capillaries were used). The sample was glued onto a glass microscope slide using UV glue on both ends. The particles in the capillary were collected into a roughly circular cluster using a small bar magnet. Finally, the sample was cleaned and placed under the microscope, with the capillary facing the lens to reduce dirt and noise in the frame. Note: using quality fresh distilled water is extremely important. Old water can get contaminated and cause particles to have close to no reaction to magnetic fields.

**Running the Experiment.** Once the sample is placed under the microscope, the magnetic field is turned on and the recording begins. Rough calculations were performed to estimate the optimal field strength, which recommended a 0.9A current (though a current of 0.07A was used for SiO 5 due to increased clustering), resulting in a field of a few milliteslas. The experimental setup is presented in Fig. 15 Immediately following the power supply, the sample began expanding as expected, though close-by particles were attracted into aggregates, and remained stuck.

We observed that particle columns tended to form when the magnetic field was turned on which can be seen in Fig. 17, creating an effective particle with larger magnetic susceptibility. We suspect that this happens since particles are on average on the same gravitational height, but when fluctuations occur and particles are slightly higher there can be attraction between two dipoles (see Eq. 3) along the  $\hat{z}$  direction causing chaining. To spread the particles out, the magnetic field was turned off and on a few times, giving the particles time to diffuse from each other thermally in between. The field was then slowly turned on. The recurring process eliminated most clusters. The attraction between close neighbors and cluster-

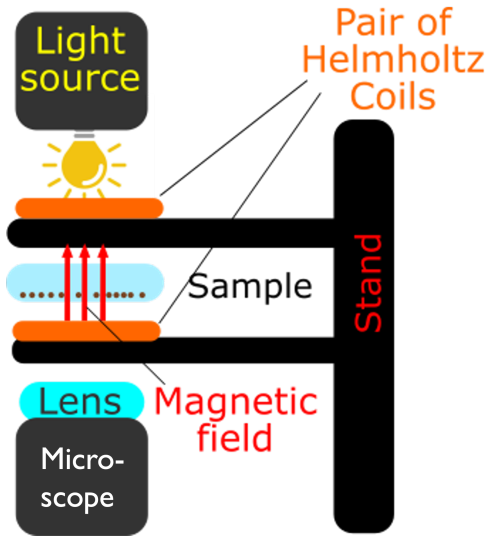


FIG. 15. The experimental setup

ing will be discussed later. It was more dominant in SiO 5, and especially in PS 5 particles, which is why the latter were not used.

In later parts of the recording, once the repulsive forces were weak enough, a drift of the sample to the left was very noticeable (see figures 23 and 24). In the latter, the camera was moved to keep the suspension in the frame, resulting in a jump in the COM). Good results were still achieved despite the drift. Most experiments lasted a couple of hours, limited by the particles reaching the border of the microscope slide.

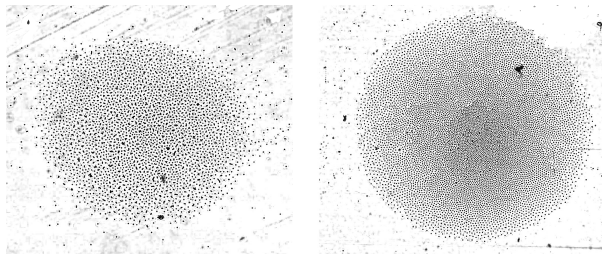
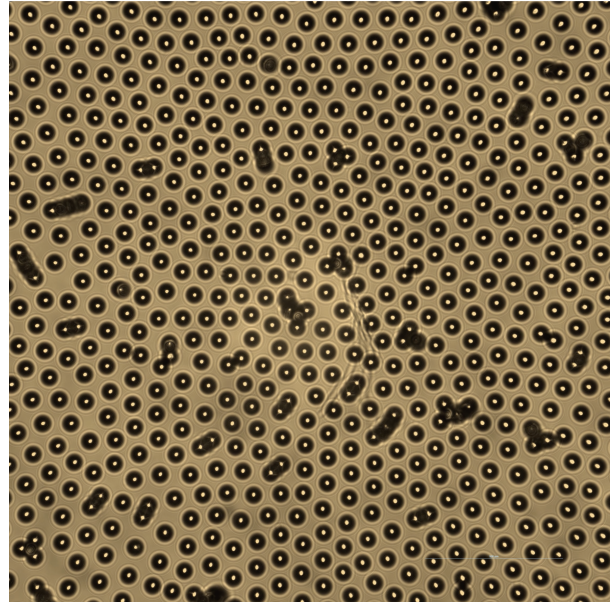
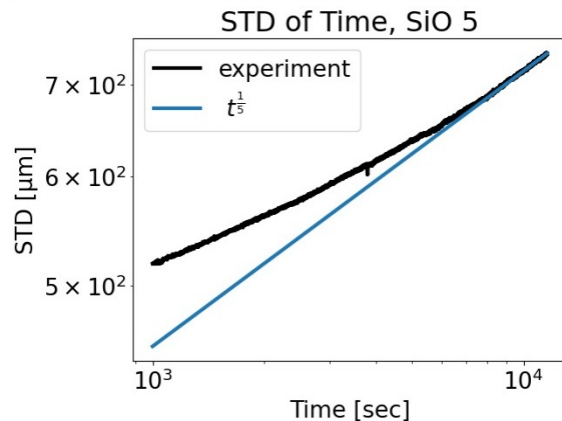


FIG. 16. A frame from each experiment. SiO 5 is on the left, and PS 10 is on the right.

**Analysis.** The results were analyzed using a python script. For each video, the code identified the particles (while ignoring stuck particles) and calculated the center of mass of the suspension. The standard deviation of the distance of the particles from the center was calculated. The density in each frame was calculated based on the Voronoi areas of the particles (a Voronoi area is all the points that are closer to the particle than to any other particle).

FIG. 17. PS particle  $10\mu\text{m}$  with  $40\times$  magnification lens, the triangular lattice as well as clustering are more visible

**Results for SiO.** Results for PS particles of diameter  $10\mu\text{m}$  were presented in the main text. Here we will present additional results for SiO particles of diameter  $5\mu\text{m}$ . The particles have a smaller magnetic susceptibility and took a much longer duration to reach the steady state distribution. Fig 18 shows agreement between theory and practice, but only after a long time because of the weak magnetic field. The standard deviation of the particles aligns with the  $R \propto t^{\frac{1}{5}}$  relation after about two hours into the experiment. Fig 19 shows the density of the suspension at a few different times.

FIG. 18. Standard deviation of the SiO  $5\mu\text{m}$  particles

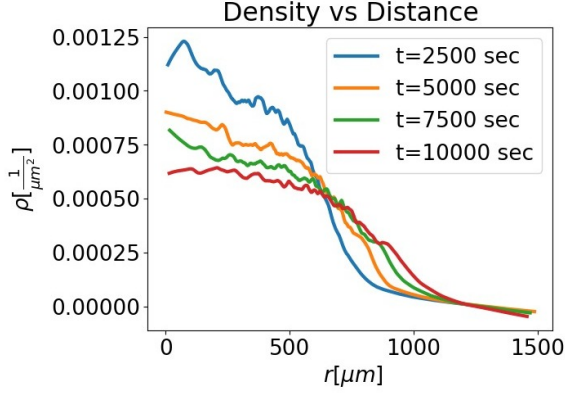
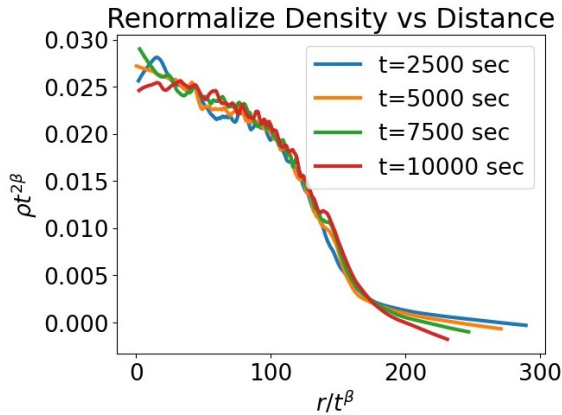
FIG. 19. Density of the SiO  $5\mu\text{m}$  particlesFIG. 20. Normalized density of the SiO  $5\mu\text{m}$  particles

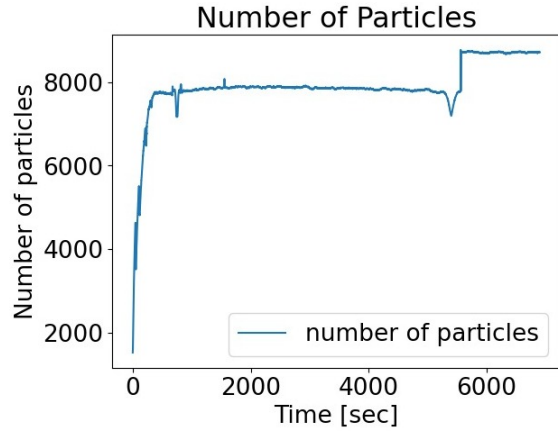
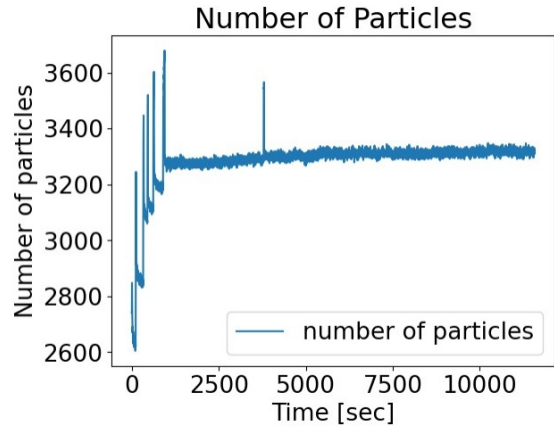
Fig 20 shows the normalized density of the suspension at a few different times. The graphs fall on the same curve, as expected.

The PS  $10\mu\text{m}$  particles reacted well to magnetic fields and did not form many clusters. For the SiO  $5\mu\text{m}$  particles, very weak magnetic fields (about 10 times weaker than those used with PS 10) were used in order to reduce the number of aggregates. Therefore, figure 18 takes a long time to stabilize. Regarding self-similarity, figure 20 demonstrates it wonderfully, and we can be confident that the system exhibits self-similar properties.

**Clustering.** According to equation 3, the magnetic field of the Helmholtz coil induces magnetic dipoles in the particles in the  $\hat{z}$  direction, resulting in positive potential energy and thus repulsion. However, due to different particle heights or non-uniformity of the field, magnetic dipoles can be induced with a component in the  $\hat{r}$  direction. Turning the field off and on resets the induced dipoles and gives the particles time to distance each other, thus

making some aggregates break apart and some stay. Fig 21 shows the amount of particles detected by the code in each frame. The number increases multiple times after turning the field off and on to eliminate clusters and stays roughly constant after a few hundred frames, up until the camera was moved.

Fig 22 and Fig. 21 show the amount of particles detected by the code in each frame. The number jumps multiple times after turning the field off and on and stays roughly constant after a few hundred frames.

FIG. 21. Number of PS  $10\mu\text{m}$  particlesFIG. 22. Number of SiO  $5\mu\text{m}$  particles

**Drift.** Drift in the sample can be observed in Fig. 23 and Fig. 24. A possible explanation is a slight tilt of the plane of the sample or magnetic fields present in the lab. Three strongly magnetized points (3-4 mT) were found inside the microscope's plate, two to the left of the suspension and one to the right. The drift is relatively slow but became noticeable a couple of hours into the experiment. Fig 23

shows the drift of the suspension in both axis, which is not insignificant. The discontinuity was caused by the repositioning of the camera. Fig 24 shows the drift of the suspension in both axes, which is not insignificant. The trend is in the same direction as in figure 23, though smaller because of a weaker magnetic field.

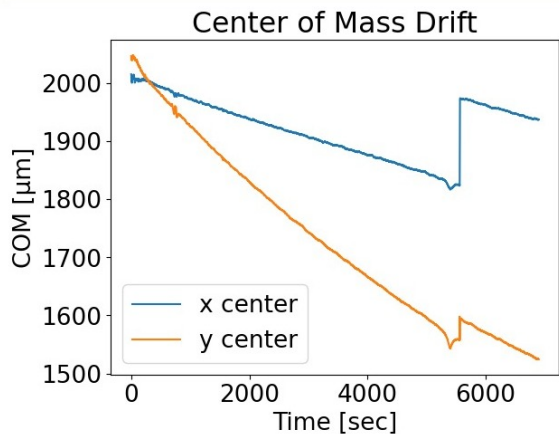


FIG. 23. Drift of the PS 10µm particles

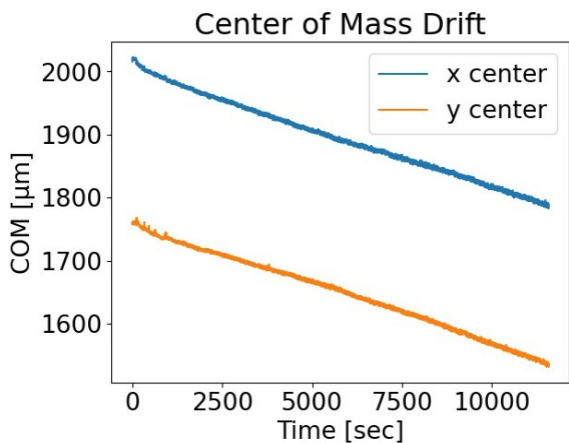


FIG. 24. Drift of the SiO 5µm particles

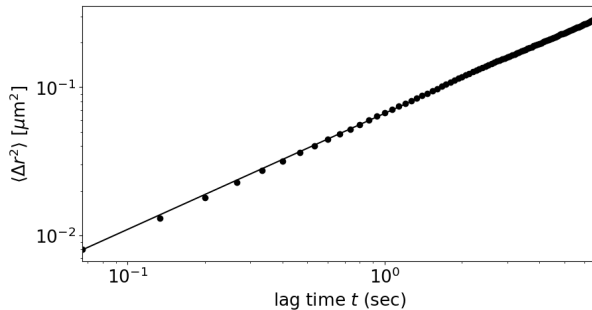


FIG. 25. MSD of the PS 10µm particles, the diffusion coefficient was found to be  $\mathcal{D} = 0.022 \left[ \frac{\mu m^2}{sec} \right]$

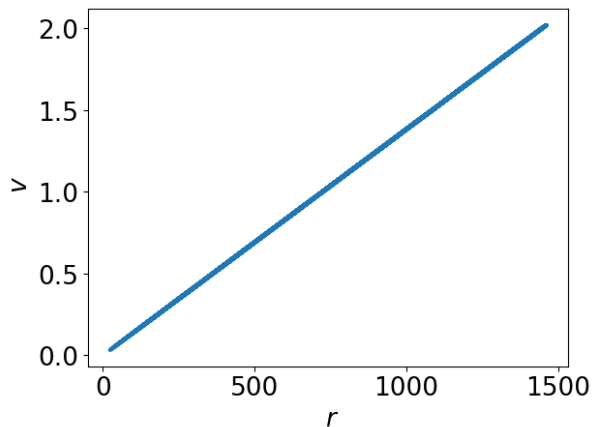


FIG. 26. velocity as a function of distance from the origin of a simulation for  $k = 0$  after 100 time steps